Journal of Materials Chemistry A

ROYAL SOCIETY OF CHEMISTRY

PAPER

View Article Online
View Journal | View Issue

Cite this: *J. Mater. Chem. A*, 2025, **13**, 14822

Multimetallic layered double hydroxides as efficient and durable oxygen evolution catalysts for anion exchange membrane water electrolysis at high current densities†

Yaowen Xu,‡[ab] Kaiyang Xu,‡[b] Hao Tan,[ab] Haoliang Huang,[b] Fei Lin,[b] Chenyue Zhang,[b] Jingwei Wang,[b] Run Ran,[b] Jinfeng Zeng,[b] Zhipeng Yu,[c] Sitaramanjaneya Mouli Thalluri,[c] Lijian Meng,[d] Dehua Xiong*[a] and Lifeng Liu*[b]

Received 28th February 2025
Accepted 31st March 2025

DOI: 10.1039/d5ta01671a

rsc.li/materials-a

The development of efficient and durable electrocatalysts for the oxygen evolution reaction (OER) is critical for advancing anion exchange membrane water electrolysis (AEMWE) technology for sustainable hydrogen production. Herein, we report the synthesis of multimetallic NiCrFeMo layered double hydroxides (LDHs) *via* a facile microwave-assisted hydrothermal approach, engineered as high-performance OER catalysts for AEMWE operating at industrially relevant current densities. Advanced X-ray absorption spectroscopy (XAS) studies demonstrate that the interplay of Ni, Cr, Fe, and Mo tailors the electronic structure and coordination environment. Consequently, the NiCrFeMo LDHs exhibit remarkable OER performance, achieving overpotentials of 236 and 387 mV at 10 and 500 mA cm^{-2}, respectively, in 1.0 M KOH, as well as outstanding durability at 500 mA cm^{-2} for 1000 hours with negligible degradation. *In situ* differential electrochemical mass spectroscopy (DEMS) and density functional theory (DFT) analyses reveal that the OER taking place on NiCrFeMo LDHs follows the adsorbate evolution mechanism, with minimal lattice oxygen involvement, contributing to the catalyst's longevity. When integrated into a prototype AEM electrolyzer cell as the anode catalyst, the cell demonstrates a current density of 1 A cm^{-2} at a relatively low voltage of 1.87 V and operates at 0.5 A cm^{-2} for 100 hours without decay, highlighting the potential of NiCrFeMo LDHs for practical applications. This work elucidates the synergistic effects of multimetallic compositions in LDHs, offering a strategy for designing cost-effective, high-efficiency OER catalysts to support green hydrogen production on scale.

1. Introduction

To meet the ever-increasing demand for energy and cope with global climate change, many countries in the world have pledged to curtail fossil fuel consumption and strived to reach carbon neutrality in the middle of the 21st century.[1] Towards this end, hydrogen (H_2) has now been broadly acknowledged to be a crucial vector during the energy transition, helping to decarbonise the transportation sector and steel and chemical industries. In particular, water electrolysis powered by renewable energy such as solar and wind, has been proposed to be the most promising approach for producing green H_2, and therefore received significant attention from both academia and industry in the past decade.[2–4] While alkaline water electrolysis (AWE) and proton exchange membrane water electrolysis (PEMWE) are currently still the predominant technologies in the market, anion exchange membrane water electrolysis (AEMWE) has emerged as a better alternative to both AWE and PEMWE, because it combines the advantages of these two technologies. For example, AEMWE does not necessarily use platinum group metals (PGMs) as the hydrogen evolution reaction (HER) and oxygen evolution reaction (OER) catalysts; moreover, it shows faster responses than conventional AWE and allows high-purity H_2 to be produced with remarkably reduced H_2/O_2 crossover due to the presence of a dense polymeric anion exchange membrane.

[a]*State Key Laboratory of Silicate Materials for Architectures, Wuhan University of Technology, Wuhan 430070, P. R. China. E-mail: xiongdehua@whut.edu.cn*

[b]*Songshan Lake Materials Laboratory (SLAB), Dongguan 523808, P. R. China. E-mail: liu.lifeng@sslab.org.cn*

[c]*International Iberian Nanotechnology Laboratory (INL), Av. Mestre Jose Veiga, 4715-330 Braga, Portugal*

[d]*Centre of Innovation in Engineering and Industrial Technology, Instituto Superior de Engenharia do Porto, Instituto Politecnico do Porto, 4249-015 Porto, Portugal*

† Electronic supplementary information (ESI) available: Fig. S1–S20, including supplementary SEM patterns, TEM and EDS images, XANES, FT-EXAFS and WT-EXAFS data, overpotential plot, CV curves, ECSA values, *in situ* Raman spectra, computation models of different catalysts, and Tables S1–S4. See DOI: https://doi.org/10.1039/d5ta01671a

‡ Y. W. X. and K. J. X. contributed equally to this work.

At present, the energy consumption of AEMWE technology remains high.[5] To address this problem, highly efficient electrocatalysts that can substantially reduce the overpotentials needed at the anode and cathode must be developed. Particularly, the OER involves four successive proton-coupled electron transfer steps and thereby exhibits slow kinetics, limiting the overall efficiency of water electrolysis.[6–10] Therefore, developing active, durable, cost-effective and PGM-free OER catalysts is of crucial importance to advance the AEMWE technology. In this respect, various materials including transition metal oxides,[11] hydroxides/oxyhydroxides.[12–15] chalcogenides,[16–18] and phosphides,[19–21] have been explored, among which layered double hydroxides (LDHs) drew considerable attention. LDHs typically exhibit a two-dimensional (2D) layered structure with a general formula of $[M_{1-x}^{2+}M_x^{3+}(OH)_2](A^{n-})_{x/n}\cdot mH_2O$, where M^{2+} and M^{3+} represent divalent and trivalent metal cations, respectively, and A^{n-} is an anion.[22,23] While early studies mainly focused on monometallic and bimetallic LDH-based OER catalysts such as $Ni(OH)_2$ and $NiFe(OH)_2$,[24,25] recent studies demonstrated that introducing multiple metals into LDHs may induce a synergistic effect between different metals, thereby improving catalytic activity.[26–28] For example, Sun *et al.* synthesised vanadium(v)-doped NiFe LDH nanosheet arrays (denoted as NiFeV LDHs) on nickel foam (NF) *via* a one-step hydrothermal method, and proved that V doping in the layered structure modulated the electronic structure, enhanced electrical conductivity and provided abundant catalytically active sites on the electrode surface, thus enabling rapid electron transfer.[29] Similarly, Xing and co-workers hydrothermally prepared NiVRu(Ir) LDHs on nickel mesh. They found that the isomorphic substitution of V by Ru (or Ir) caused lattice distortion and the formation of V vacancies, resulting in synergistic interaction among all cations and therefore enhanced OER performance.[30]

The selection of metal components in multimetallic LDHs is important to design high-performance LDH-based catalysts. It is well known that $Ni(OH)_2$ is particularly active for alkaline OER and has long been used for alkaline water electrolysis.[31,32] Bell *et al.* employed *in situ* Raman spectroscopy to monitor the structural transformation of $Ni(OH)_2$ catalysts with increasing applied potential,[33] and confirmed that Ni^{3+} species in the formed NiOOH are the true catalytically active sites. Despite reasonably good OER activity, NiOOH itself is not electrically conductive, therefore often resulting in poor charge transfer properties.[34,35] To address this issue, many researchers have managed to introduce Fe into Ni-based LDHs. For example, Boettcher and co-workers demonstrated that the incorporation of Fe into NiOOH lattices improves the electronic conductivity of the catalyst.[36] Additionally, Fe can induce a partial charge transfer activation effect on Ni centres, leading to enhanced OER activity. However, such enhancements could not be fully explained by this effect alone, suggesting that other factors, such as structural changes or synergistic interactions between Ni and Fe, may also contribute to the improved activity.[36] To this end, Peng *et al.* also proved through *in situ* and *ex situ* X-ray absorption spectroscopy (XAS) that Fe^{2+} species can promote the cycling of Ni and Co between their 2+ and 3+ oxidation states, thereby boosting the OER activity.[37]

While NiFe LDHs have demonstrated superior activity towards the OER,[38] their electrocatalytic stability is still a major concern, particularly at high current densities. To tackle this problem, Xu *et al.* tried to incorporate Cr into NiFe oxide/(oxy)hydroxide catalysts.[39] They found that Cr gradually leached out during the OER. Nevertheless, the OER activity of the catalysts got stabilised, due to the creation of new nanopores and/or active sites that can compensate for the Cr-leaching induced activity loss. Moreover, Tang and co-workers demonstrated through *ex situ*/*in situ* microscopic and spectroscopic characterisation that Cr species (incl. Cr(III) and Cr(VI)) dispersed on NiFe LDH nanosheets could significantly enhance catalytic stability in harsh seawater electrolytes. They proposed that the highly dispersed nanosized Cr_2O_3 acts as the Lewis acid sites that can enrich the local OH^- concentration, thereby creating a favourable surface microenvironment with strong adsorption affinity towards OH^-.[40] Besides, high-valence metals, owing to their high electronegativity and unique physicochemical properties,[41,42] have also been explored to improve the stability of LDHs through electronic structure modulation. For example, Kuepper *et al.* demonstrated that the incorporation of high-valence Mo can help stabilise the otherwise unstable low-charge Fe^{2+} during the OER.[43] Furthermore, Yang *et al.* successfully synthesised FeCoMo LDHs and demonstrated through *in situ* X-ray absorption near-edge structure (XANES) spectroscopy that during the OER, Mo^{6+} tends to attract electrons to increase the valence states of 3d metals, promoting the OER.[44] Considering that molybdenate is the most commonly used precursor for the preparation of LDHs containing Mo, the intercalation of MoO_4^{2-} into the layered structure may expand the interlayer spacing and facilitate the diffusion of water molecules and OH^- anions, therefore enabling the OER to proceed *via* the favourable adsorbate evolution mechanism. Although some progress has been made in doped LDH OER catalysts, combining the aforementioned strategies to design NiCrFeMo multimetallic LDHs with both high OER activity and stability, capable of working at high current densities relevant to industrial applications, has not been reported yet.

In this work, we report the synthesis of multimetallic LDH catalysts consisting of inexpensive transition metals Ni, Cr, Fe and Mo, through a facile microwave-assisted hydrothermal method. Our comprehensive XAS studies confirmed the subtle interaction among all metal species in NiCrFeMo LDHs, which offers a favourable electronic structure for the OER. When compared to other control bimetallic and trimetallic LDH catalysts synthesised using the same method, the NiCrFeMo LDHs exhibited outstanding OER performance, only requiring overpotentials of 236, 301, and 387 mV to attain current densities of 10, 100, and 500 mA cm^{-2}, respectively. In particular, NiCrFeMo LDHs could continuously catalyse the OER at 500 mA cm^{-2} for 1000 h without degradation, outperforming many LDH-based OER catalysts reported to date. Our *in situ* differential electrochemical mass spectroscopy (DEMS) measurements and density functional theory (DFT) calculations reveal that the OER taking place on NiCrFeMo LDHs prefers to proceed through the adsorbate evolution mechanism with

a smaller energy barrier in the rate-determining step, and lattice oxygen does not participate in the OER, thereby enabling NiCrFeMo LDHs to have both high activity and good stability. Furthermore, we demonstrated that NiCrFeMo LDHs exhibit excellent performance in a prototype AEMWE when used as the anode catalysts. The electrolyser cell can achieve 1 A cm^{-2} at a voltage of 1.87 V and operate at 0.5 A cm^{-2} for 100 h without notable performance decay, showing substantial potential for practical applications.

2. Materials and methods

2.1 Chemicals and materials

Sodium molybdate dihydrate ($Na_2MoO_4 \cdot 2H_2O$), nickel chloride hexahydrate ($NiCl_2 \cdot 6H_2O$), iron chloride hexahydrate ($FeCl_3 \cdot 6H_2O$), and ammonium fluoride (NH_4F) were purchased from Macklin. Chromium chloride hexahydrate ($CrCl_3 \cdot 6H_2O$) was bought from Aladdin. Urea was obtained from Innochem. Nafion® perfluorinated resin solution (5 wt%) was purchased from Alfa Aesar. Potassium hydroxide (KOH) was acquired from Sinopharm Chemical Reagent Co. Ethanol (C_2H_6O, ≥99.7%), hydrogen peroxide (H_2O_2, 30%) and nitric acid (HNO_3, analytical pure) were bought from Xilong Scientific. $H_2{}^{18}O$ (99.0%) was purchased from Energy Chemical. Hydrophilic carbon paper was ordered from SCI Materials Hub. Conductive carbon black was produced by CABOT. A 600-mesh high-purity nickel mesh was bought from Kunshan Jinanjia New Materials Co., Ltd. All reagents and materials were used as received without further purification. Deionized (DI) water with a resistivity value of 18.2 MΩ cm was employed to prepare all solutions and electrolytes.

2.2 Synthesis of LDH catalysts

The NiCrFeMo LDHs were synthesised through a microwave-assisted hydrothermal process. Specifically, $NiCl_2 \cdot 6H_2O$, $CrCl_3 \cdot 6H_2O$, $FeCl_3 \cdot 6H_2O$, and Na_2MoO_4 (1.25 mmol of each chemical) were dissolved in 60 mL of DI water, and the mixture was stirred at room temperature for 30 min. Subsequently, 20 mmol of urea and 10 mmol of NH_4F were added into the mixture, which was then continuously stirred at room temperature for another 30 min. Afterwards, the solution was transferred to a 100 mL reaction vessel. The hydrothermal synthesis was conducted at 160 °C (heating rate: 12 °C min^{-1}) for 2 h with a microwave power of 1800 W (fluctuation <1%). After this, the reactor was naturally cooled down to room temperature, and the powders were collected and thoroughly washed with DI water and ethanol in sequence four times. Finally, the obtained powders were dried in a vacuum oven at 60 °C for 12 h.

To make a comparison, other control catalysts including NiCrFe LDHs, NiCrMo LDHs, and NiCr LDHs were also prepared in a similar way. The experimental parameters used are summarised in Table S1 (ESI).†

2.3 Materials characterisation

To investigate the crystal phase of as-prepared LDH catalysts, X-ray diffraction (XRD) examination was performed on a Panalytical Aeris diffractometer with Cu K_α radiation (λ = 0.15406 nm, current: 7.5 mA, voltage: 40 kV) at a scan rate of 0.04° s^{-1} in the 2θ range of 10°–90°. Fourier transform infrared spectroscopy (FTIR, PerkinElmer Frontier) was used to examine the molecule structure in the range of 4000–400 cm^{-1}. The actual metal contents in LDH-based catalysts were determined by inductively coupled plasma – optical emission spectroscopy (ICP-OES, Thermo Scientific TM iCAP TM 7200), and the metal dissolution upon long-term stability tests was detected by inductively coupled plasma – mass spectrometry (ICP-MS, Agilent Technologies Agilent 7900). The morphology of LDHs was examined using a benchtop scanning electron microscope (SEM, Thermo Scientific Phenom ProX) at an acceleration voltage of 5 kV and a field-emission scanning electron microscope (FESEM, ZEISS/Gemini 300 EBSD) at 15 kV. Transmission electron microscopy (TEM) and high-angle annular dark-field scanning TEM (HAADF-STEM) were carried out on a JEOL JEM F200 microscope equipped with an energy-dispersive X-ray spectrometer (EDS) at 200 kV. X-ray photoelectron spectroscopy (XPS) was conducted on a Thermo Fisher Scientific K-Alpha spectrometer with Al-K_α radiation (1486.6 eV). X-ray absorption near-edge structure (XANES) and extended X-ray absorption fine structure (EXAFS) spectra were acquired at B18 beamline, Diamond Light Source, UK.

2.4 Electrochemical measurements

The electrocatalytic tests were performed in the three-electrode configuration using a Biologic electrochemical workstation (VMP3e). To prepare the catalyst ink, 90 mg of the as-prepared catalyst, 36 mg of acid-treated carbon black, 8.82 mL of isopropanol, 9 mL of DI H_2O, and 270 μL of 5 wt% Nafion® solution were mixed and sonicated for 120 min. Subsequently, the ink was spray-coated onto a piece of 3 × 3 cm^2 600-mesh nickel mesh with a loading density of 1.8 ± 0.05 mg cm^{-2}. The catalyst-coated nickel mesh served as the working electrode, and a graphite rod and a Hg/HgO electrode were used as the counter and reference electrodes, respectively. The OER performance was assessed in a 1.0 M KOH solution in an electrochemical cell soaked in a water bath with controlled temperature (25 ± 2 °C). Linear sweep voltammetry (LSV) curves were recorded in the potential range of 1.22–1.72 V *vs.* the reversible hydrogen electrode (RHE) at a scan rate of 5 mV s^{-1}, under constant magnetic stirring (600 rpm). 85% *iR* compensation was applied during the acquisition of the curves to automatically correct the potential drop caused by inherent resistance of the testing cell. The recorded potential was converted to the one on the RHE scale as follows:[45]

$$E_{RHE} = E_{Hg/HgO} + 0.098 + 0.0592 \times pH \quad (1)$$

The Tafel slope was derived from the LSV curve according to the following equation:[46]

$$\eta = a + b \log j \quad (2)$$

where η is the overpotential, b stands for the Tafel slope, j represents the current density, and a denotes the exchange

current density. The electrochemical impedance spectroscopy (EIS) measurements were performed at 1.471 V *vs.* RHE in the frequency range of 10^5–10^{-2} Hz with a 5 mV sinusoidal perturbation. The electrochemical double-layer capacitance (C_{dl}) was measured in the non-Faraday potential region of 1.04–1.14 V *vs.* RHE using cyclic voltammetry (CV) at various scan rates of 20, 40, 60, 80, 100 and 120 mV s^{-1}, respectively. The C_{dl} value was obtained by fitting the difference between the anodic and cathodic current densities against the scan rate at 1.09 V *vs.* RHE, and then dividing by two. Based on the obtained C_{dl} values, the electrochemically active surface area (ECSA) of catalysts was estimated according to the following equation:[47]

$$\mathrm{ECSA} = C_{dl}/C_s \quad (3)$$

where C_s is the specific capacitance of the sample, which is assumed to be 0.04 mF cm^{-2} for oxide surfaces in alkaline media according to previous reports.[48] Electrochemical stability of LDH-based electrocatalysts was evaluated using CV and chronopotentiometry (CP).

2.5 *In situ* differential electrochemical mass spectroscopy (DEMS) measurements

DMES measurements were performed on a Hiden HPR-40 electrochemical differential mass spectrometer equipped with a CHI-660e electrochemical workstation. A piece of catalyst-loaded porous carbon paper, a Hg/HgO electrode and a platinum (Pt) wire were used as the working, reference and counter electrodes, respectively. To obtain similar current densities, the CV potential ranges of NiCrFeMo LDHs were set to 1.05–1.55 V *vs.* RHE. The catalyst was labelled with the ^{18}O isotope by performing 20 CV cycles at 5 mV s^{-1} in 0.1 M KOH prepared with $H_2{}^{18}O$. After this, the electrochemical cell was carefully rinsed with 0.1 M KOH containing $H_2{}^{16}O$ ten times to ensure complete removal of any residual $H_2{}^{18}O$. Subsequently, the cell was filled with 0.1 M KOH prepared with $H_2{}^{16}O$, and CV was performed under the same conditions as described above. A porous polytetrafluoroethylene (PTFE) membrane was used at the bottom of the cell as the interface between the solution and the vacuum for gas–liquid separation. The O_2 produced during the electrochemical tests was probed synchronously by mass spectrometry.

2.6 DFT calculations

First-principles DFT calculations were carried out using a generalized gradient approximation with the Perdew–Burke–Ernzerhof exchange correlation functional. The projector-augmented wave method was used to describe ionic cores as implemented in the Vienna *ab initio* simulation package (VASP). The wave functions were constructed from the expansion of plane waves with an energy cutoff of 500 eV. A gamma centred *k*-point mesh of 3 × 3 × 1 was employed for geometry optimisation. The consistency tolerances for geometry optimisation were set to 1.0×10^{-5} eV per atom for total energy and 0.05 eV $Å^{-1}$ for force, respectively. In order to avoid the interaction between the two surfaces, a large vacuum gap of 30 Å was inserted between the periodically repeated slabs.

In an alkaline environment, the Gibbs free energy of the adsorbed substance can be calculated as:

$$\Delta G = E_{ads} + \Delta E_{ZPE} - T\Delta S + eU \quad (4)$$

where E_{ads} is the adsorption energy of the intermediate, ΔE_{ZPE} represents the zero-point energy difference between the adsorption state and gas state, T denotes the temperature, and ΔS stands for the entropy variation between the adsorption and gas phase. For adsorbates, E_{ZPE} and S values were obtained from vibrational frequency calculations with the harmonic approximation, and the contributions from the slabs were neglected. Similarly, for H_2O and H_2 molecules these values were also computed from their vibrational frequencies. Additionally, the energy of the oxygen molecule was calculated using the following method:

$$E_{O_2} = 2E_{H_2O} - 2E_{H_2} \quad (5)$$

The following reaction steps were considered during the OER to calculate the Gibbs energy changes based on the adsorbate evolution mechanism:[49]

$$* + OH^- \rightarrow *OH + e^- \quad (6)$$

$$*OH + OH^- \rightarrow *O + H_2O + e^- \quad (7)$$

$$*O + OH^- \rightarrow *OOH + e^- \quad (8)$$

$$*OOH + OH^- \rightarrow * + O_2\uparrow + H_2O + e^- \quad (9)$$

where * denotes the active site on the catalyst surface.

Besides, the lattice oxygen mechanism (LOM) was also considered, which includes the following five steps:[50]

$$*O_1H + OH^- \rightarrow *O_1 + H_2O + e^- \quad (10)$$

$$*O_1 + OH^- \rightarrow *O_1OH + e^- \quad (11)$$

$$*O_1OH + OH^- \rightarrow *O_1O + H_2O + e^- \quad (12)$$

$$*O_1O \rightarrow * + O_2\uparrow \quad (13)$$

$$* + OH^- \rightarrow *O_1OH + e^- \quad (14)$$

where * represents the vacancy site and O_1 denotes the lattice oxygen atom.

2.7 Electrochemical tests in membrane electrode assemblies (MEAs)

The OER performance of NiCrFeMo LDHs and their potential for use in AEMWE were further evaluated in MEAs. Specifically, the catalyst, acid-treated carbon black and Nafion® solution (mass ratio – $m_{catalyst} : m_{Nafion} : m_{carbon} = 35.4 : 5.0 : 14.2$) were dispersed in a mixture containing H_2O and isopropanol (V_{H_2O}: $V_{IPA} = 1 : 1$). After ultrasonication for 120 min, a homogeneous catalyst ink was obtained, which was then sprayed onto a 600-

mesh nickel current collector at 80 °C as the anode. Commercial Pt/C (TKK, 40 wt% Pt) was employed as the cathode catalyst for H_2 evolution. The Pt/C ink was prepared in a similar way to that described above and then sprayed on a piece of carbon paper (Pt/C@C) as the cathode. A piece of PiperION A20 was used as the anion exchange membrane. The area of catalyst layers was 1 cm × 1 cm for both the anode and the cathode, with the NiCrFeMo LDH and Pt/C loadings being 1.8 ± 0.05 mg_{cat} cm^{-2} and 1.12 $mg_{Pt/C}$ cm^{-2}, respectively. A porous Ti@Au felt and a Ti@Pt felt were utilized as the porous transport layer (PTL) at the cathode and anode, respectively. PTFE membranes were employed as the gaskets placed between the electrode and the PTL, with the cathode and anode gasket thickness being 0.2 mm and 0.1 mm, respectively. A single-cell AEM electrolyser was then obtained by assembling a PiperION A20 membrane sandwiched by the anode and cathode, followed by the Ti@Au and Ti@Pt PTLs and finally the end plates with flow fields, altogether. After the assembly, screws were carefully tightened using a torque wrench with a fixed applied torque of 8 N m. The steady-state polarisation curve was recorded in the galvanostatic mode from 0 to 1 A cm^{-2}, and the stability was assessed at a constant current density of 0.5 A cm^{-2}. The cell temperature was maintained at 80 °C during the tests, and all data are presented as acquired without *iR* correction.

3. Results and discussion

3.1 Physicochemical characterisation of LDH catalysts

Fig. 1a shows the XRD patterns of the as-prepared samples. All samples exhibit diffraction peaks at around 18.8°, 36.4°, 46.5°, and 61.6°, which can be assigned to the (003), (012), (015), and (009) crystal planes, respectively, of hexagonal CrOOH (JCPDS No. 09-0331). It is noted that these diffraction peaks shift towards lower angles, compared to the standard diffraction pattern of CrOOH, indicating that the lattice distance in the synthesised LDHs expands. While NiCr LDHs show a good crystallinity, increasing the number of metals in LDHs causes the broadening of diffraction peaks, which suggests an enhancement in the amorphous nature of the samples.[51] In particular, with the incorporation of Mo, the diffraction peaks remarkably broaden. This likely results from the lattice distortion induced by the substitution of high-valence Mo cations for Ni, Cr, and/or Fe, which increases the disorder of the lattice. It is expected that such amorphous LDHs may offer higher OER activity owing to their flexible structure and abundant unsaturated coordination sites, which facilitate the adsorption of reactants.[52] Additionally, the functional groups of the LDHs were analysed using FTIR spectroscopy. The vibrational bands located at 3304, 1632, and 1357 cm^{-1} are assigned to signals from –OH, H_2O, and CO_3^{2-} groups (Fig. 1b), respectively.[53] The –OH and CO_3^{2-} are typical interlayer anions in LDHs, with CO_3^{2-} originating from the decomposition of urea, confirming the successful preparation of the LDH materials. Fig. 1c shows the ICP-OES results of all catalysts. Ni, Cr and Fe exhibit reasonably good equimolar stoichiometry. However, the Mo content is found to be notably lower than that of other elements, likely due to the larger atomic radius of Mo that makes it more difficult to be incorporated into the structure.

Furthermore, the morphology of LDH catalysts was examined by SEM. Fig. 1d shows a representative SEM image of NiCrFeMo LDHs, where aggregates of numerous irregular spherical particles are observed. Compared to other LDH samples (Figs. S1a, S2a, and S3a, ESI†), the size of primary NiCrFeMo LDH particles looks smaller, which would be more favourable for catalytic reactions. Fig. S4 (ESI)† displays high-magnification FESEM images of all samples, in which the smaller size of NiCrFeMo LDHs can be more clearly discerned. Fig. 1e shows a typical TEM image of NiCrFeMo LDHs showing a nanoporous morphology comprised of numerous layered nanoflakes. Interestingly, NiCr, NiCrFe, and NiCrMo LDHs do not exhibit a similar architecture, and the nanospheres observed in these samples are solid in bulk (Fig. S1–S3, ESI†). Upon a closer look at NiCrFeMo LDHs using high-resolution TEM (HRTEM), we found that they are composed of many tiny crystallites of few nanometres embedded in an amorphous matrix (Fig. 1f), implying that there is only short-range order in the lattice, consistent with the XRD result mentioned above. The measured interplanar fringe is 2.01 Å, in line with the lattice distance of the (104) crystal plane of CrOOH (JCPDS No. 09-0331). The selected-area electron diffraction (SAED) pattern shows three weak, diffusive rings that can be assigned to the (012), (104) and (009) planes. Furthermore, the elemental maps of NiCrFeMo LDHs were acquired by HAADF-STEM, and Ni, Cr, Fe, and Mo elements reveal a uniform distribution across the whole area under investigation (Fig. 1g).

XPS characterisation was further carried out to study the surface composition and electronic states of LDH-based catalysts. The presence of corresponding metal elements in each sample was confirmed by the survey spectrum (Fig. 2a), which agrees well with the EDS results. Fig. 2b shows the high-resolution Ni 2p spectra of all samples, which are very similar. There are two dominant peaks observed at binding energies of 856.1 and 873.7 eV, corresponding to the $2p_{3/2}$ and $2p_{1/2}$ components of Ni^{2+} species, respectively. Additionally, satellite peaks also appear at 862.1 and 880.1 eV.[54–56] In the Cr 2p spectra (Fig. 2c), all samples also show similar $2p_{1/2}$ and $2p_{3/2}$ components. Peak fitting reveals that the signals at 586.8 and 577.1 eV are attributed to Cr^{3+} hydroxides, while those at 589.9 and 580.1 eV are associated with Cr^{3+} oxides.[57] As for Fe 2p spectra, characteristic Fe $2p_{3/2}$ and Fe $2p_{1/2}$ components are observed at 711.9 and 725.2 eV (Fig. 2d), respectively, accompanied by satellite peaks at 717.9 eV and 732.9 eV, confirming the presence of Fe^{3+} species in LDHs.[58] Furthermore, Mo $3d_{3/2}$ and Mo $3d_{5/2}$ components are observed at 235.4 and 232.3 eV, respectively (Fig. 2e), in the Mo 3d spectra of two Mo-containing LDHs, indicating that Mo in these samples is present in a high-valence oxidation state of +6.[59] Besides, the high-resolution O 1 s spectra of all samples are also analysed (Fig. 2f), which can be deconvoluted into three characteristic peaks corresponding to H–O–H, metal−OH (M–OH), and metal–O–metal (M–O–M) bonds. For all samples, the signal from M–OH is predominant, typical of LDH-based materials.[60] It is also noted that the introduction

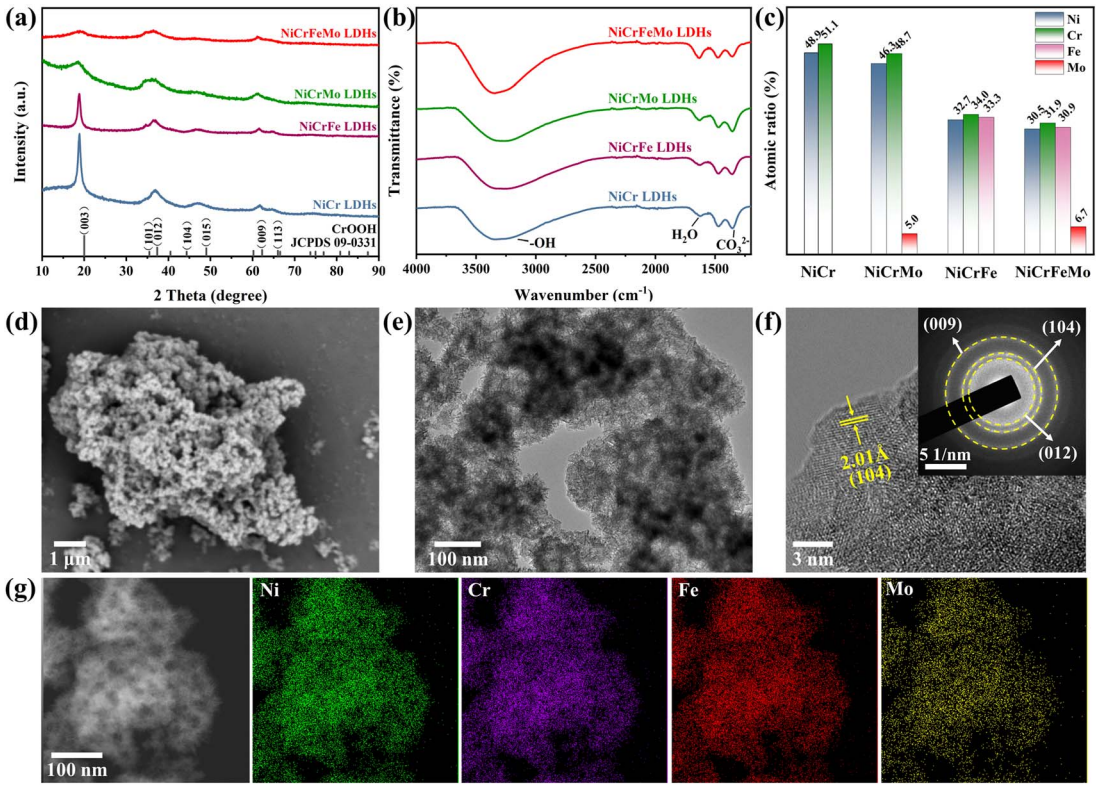

Fig. 1 (a) XRD patterns, (b) FTIR spectra, and (c) ICP-OES data of NiCrFeMo LDHs and other controls. (d) SEM, (e) TEM and (f) HRTEM images of NiCrFeMo LDHs. Inset of (f): SAED pattern. (g) TEM-EDS elemental maps of NiCrFeMo LDHs.

of Mo into LDHs promotes the formation of M–O bonds,[61] as evident from the XPS spectra of NiCrMo and NiCrFeMo LDHs.

To further elucidate the local electronic structure and coordination environment of the prepared LDHs, synchrotron-based XANES and Fourier transform EXAFS (FT-EXAFS) spectroscopy measurements were conducted. The Ni K-edge XANES spectra show that the oxidation state of Ni in the as-prepared LDHs is similar to that in the $Ni(OH)_2$ reference (Fig. 2g), indicating that Ni primarily exists in the Ni^{2+} oxidation state. Nevertheless, all LDHs exhibit a slight positive shift upon a closer look (Fig. 2g inset), suggesting that the oxidation state is actually >2+. Fig. S5a† presents the Cr K-edge XANES spectra of all samples. The Cr chemical state in the as-prepared samples is close to that in the Cr_2O_3 standard, confirming that Cr is predominantly present in the form of Cr^{3+}. Likewise, a slight positive shift is observed for all LDHs with respect to the Cr_2O_3 benchmark. Additionally, the Cr K-edge in NiCrFe LDHs blueshifts slightly compared to that in NiCr LDHs, and the same is observed for NiCrFeMo LDHs relative to NiCrMo LDHs (Fig. S5a inset, ESI†). This implies that the introduction of Fe elevates the oxidation state of Cr. Conversely, the Cr K-edge in NiCrMo LDHs exhibits a slight redshift compared to that in NiCr LDHs, and the Cr K-edge in NiCrFeMo LDHs shows a similar redshift with respect to that in NiCrFe LDHs, suggesting that the incorporation of high-valence Mo reduces the oxidation state of Cr. As for the XANES spectra of Fe, it is found that the Fe chemical state in the LDH samples resembles that in Fe_2O_3 (Fig. S5b, ESI†), manifesting that Fe mainly exists in the Fe^{3+} oxidation state. Moreover, the Fe K-edge in NiCrFeMo LDHs exhibits a slight redshift relative to that in NiCrFe LDHs, again corroborating that the introduction of Mo tends to lower the oxidation state of Fe. Fig. S5c (ESI)† displays the Mo K-edge spectra, where it is observed that the oxidation state of Mo in the LDHs is close to that in MoO_3, which suggests that Mo is primarily present in the Mo^{6+} oxidation state. Compared to NiCrMo LDHs, NiCrFeMo LDHs show a little blueshift in the K-edge, indicating that Fe increases the oxidation state of Mo. Overall, the XANES analyses confirm that the oxidation states of metal elements agree with the XPS analyses and are also in line with those of metal salt precursors used to prepare LDHs. Significantly, we found that the introduction of Fe helps to increase the oxidation state of other metal elements, while the introduction of high-valence Mo tends to decrease the oxidation state of other metals. The XANES results unambiguously illustrate that the oxidation states of metal elements in LDHs can be fine-tuned by selectively introducing specific elements.

Fig. 2h and S6 (ESI)† show the FT-EXAFS spectra of all LDH catalysts. The profiles of all metal elements in different materials (*i.e.*, NiCr, NiCrFe, NiCrMo, and NiCrFeMo) are similar, indicating they have similar local coordination environments. To better decipher the local bonding environment from these spectra, wavelet transform (WT) EXAFS analysis was carried out. As shown in the Ni K-edge WT-EXAFS contours (Fig. 2i), all LDHs show a maxima in k space centred at 4.63 $Å^{-1}$,

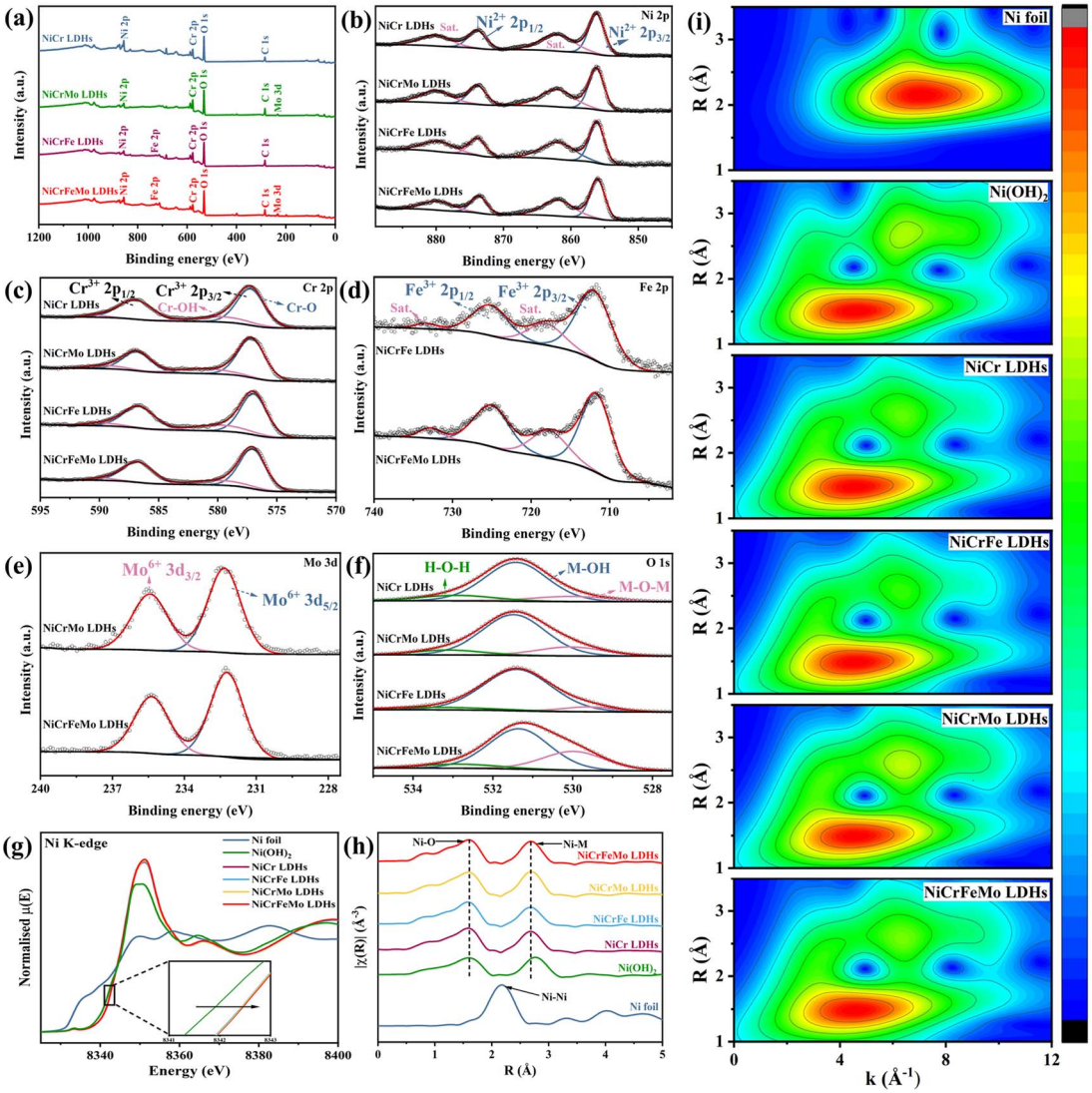

Fig. 2 (a) XPS survey spectra and high-resolution (b) Ni 2p, (c) Cr 2p, (d) Fe 2p, (e) Mo 3d, and (f) O 1s XPS spectra of all LDH catalysts under investigation. (g) Ni K-edge XANES spectra. (h) Fourier transforms of the k^2 weighted EXAFS oscillations in R-space. (i) Wavelet transform contour maps of the Ni K-edge EXAFS, derived from different LDHs.

corresponding to the Ni–O bonding.[62] Moreover, the introduction of Mo results in an increase in the scattering intensity at 6.40 $Å^{-1}$ that is attributed to the Ni–M coordination, whereas the addition of Fe exhibits an adverse influence on the Ni–M signal. The WT-EXAFS contours of Cr, Fe, and Mo show insignificant differences in scattering intensity for all LDHs, indicating that their local coordination environments are quite similar and cannot be readily changed by foreign elements (Fig. S7, ESI†).

To quantitatively analyse the coordination environment in LDH catalysts, the EXAFS spectral fitting was carried out (Fig. S8 and Table S2, ESI†). The coordination number (CN) of Ni–O bonding in all LDHs is close to 6, confirming that these LDHs adopt a hexagonal structure. When comparing NiCr to NiCrFe and NiCrMo to NiCrFeMo, it is found that the introduction of Fe virtually does not change the bond length of Ni–O. In contrast, the Mo incorporation obviously increases the Ni–O bond length, from 2.048 to 2.054 for both NiCrMo relative to NiCr and NiCrFeMo relative to NiCrFe (Table S2, ESI†), suggesting that the introduced Mo lowers the metal oxidation state, which is consistent with the above XANES analysis.

Overall, our XAS data imply that the incorporation of Fe and Mo into LDHs induces opposing changes in the electronic structure and local coordination environment, which may result in optimal conditions for the OER to occur.

3.2 Electrocatalytic performance

The OER performance of the as-prepared LDH catalysts was evaluated in 1.0 M KOH using a three-electrode system. For comparison, the OER performance of commercial RuO_2 was also tested under the same conditions. As shown in Fig. 3a, NiCrFeMo LDHs show the best OER performance among all catalysts under investigation, only requiring an overpotential of

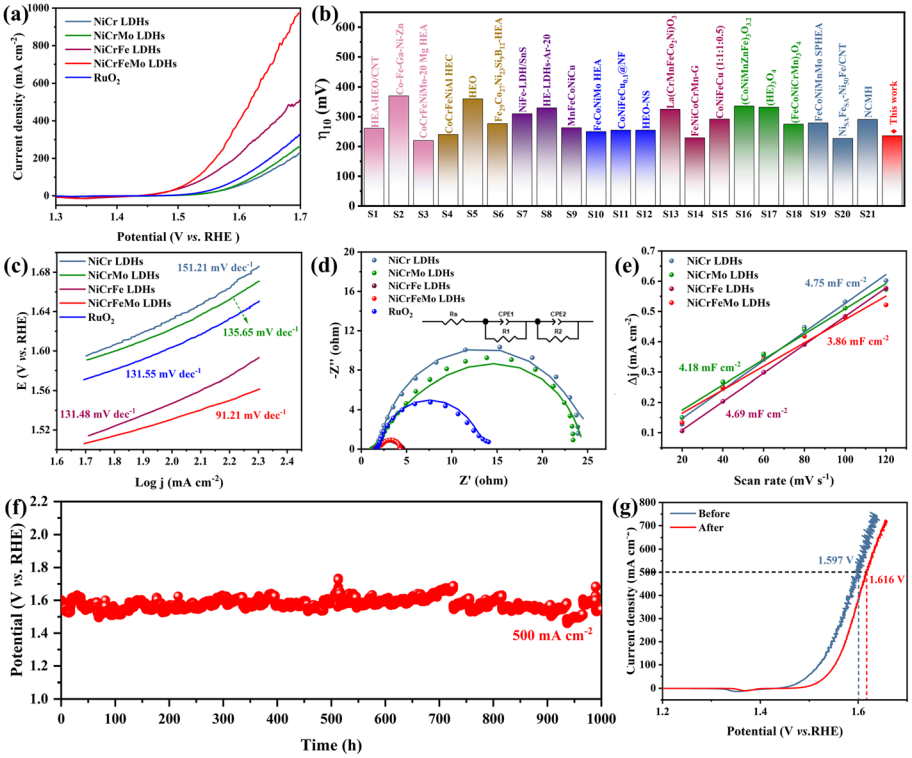

Fig. 3 (a) The OER polarisation curves of the as-prepared LDH catalysts and RuO_2 control. (b) Comparison of the overpotentials required at 10 mA cm^{-2} for the NiCrFeMo LDHs (this work) with other recently reported electrocatalysts. The number below the horizontal axis indicates the number of references presented in the ESI.† (c) Tafel plots and (d) Nyquist plots of different LDHs and the RuO_2 control. The scattered dots are experimental data, and the solid lines represent fitting curves. Inset: the equivalent circuit model. (e) Double-layer capacitance (C_{dl}) of various LDH catalysts. (f) Chronopotentiometric curve of the NiCrFeMo LDHs recorded at 500 mA cm^{-2}. (g) The polarisation curves of NiCrFeMo LDHs before and after the long-term stability test.

236 mV (η_{10}) to deliver a current density of 10 mA cm^{-2}, even better than that of noble metal based RuO_2 catalysts (η_{10} = 290 mV). Specifically, at a high current density of 500 mA cm^{-2}, NiCrFeMo LDHs exhibit an overpotential of 387 mV (Fig. S9, ESI†), which is markedly lower than that of NiCrFe LDHs (467 mV) and RuO_2 (531 mV). Moreover, as shown in Fig. 3b, the OER activity of NiCrFeMo LDHs is also favourably comparable to that of many other alloy and oxide based OER catalysts as well as multimetallic LDHs reported recently in the literature (see Tables S3 and S4 for details, ESI†).

The electrocatalytic reaction kinetics were evaluated using Tafel plots derived from polarisation curves. As shown in Fig. 3c, the Tafel slope of NiCrFeMo LDHs is 91.21 mV dec^{-1}, significantly lower than that of other LDH catalysts, indicating faster OER kinetics. The EIS measurements revealed that the charge transfer resistance (R_{ct}) of NiCrFeMo LDHs is the lowest among that of all samples (Fig. 3d), indicating their fastest charge transfer rate in the OER process, consistent with the Tafel analysis. Furthermore, the electrochemically active surface area (ECSA) of different samples was estimated based on the double-layer capacitance (C_{dl}) in the non-faradaic potential region (1.04–1.14 V *vs.* RHE, Fig. S10a–d, ESI†). The C_{dl} value for NiCrFeMo LDHs was calculated to be 3.86 mF cm^{-2}, which is smaller than that of other catalysts (Fig. 3e), leading to a lower ECSA (Fig. S10e, ESI†). This implies that the high OER performance of NiCrFeMo LDHs cannot be simply ascribed to their accessible surface area. Instead, the unique combination of these quaternary elements results in intrinsically high activity and makes a major contribution to the observed outstanding OER performance, as will be discussed in the following section in detail.

Furthermore, the electrocatalytic stability of NiCrFeMo LDHs was assessed using chronopotentiometry (CP) at 500 mA cm^{-2}. NiCrFeMo LDHs can sustain continuous OER electrocatalysis at such a high current density for 1000 h with a minimal degradation of only 30 mV (Fig. 3f), corresponding to a decay rate of ~0.05 mV h^{-1}, which demonstrates excellent long-term stability. Moreover, the polarisation curves recorded before and after the stability test are comparable (Fig. 3g), and only a slight positive shift is observed.

Furthermore, the phase and microstructure of the NiCrFeMo LDH catalysts after the extended stability test at 500 mA cm^{-2} were examined. Fig. 4a shows the XRD patterns of the NiCrFeMo LDHs loaded on the Ni mesh current collector before and after the CP test. Besides the strong diffractions originating from the Ni mesh (marked with yellow hearts), new peaks at 11.7°, 23.1°, and 34.8° emerge in the sample after the test (denoted as "CP-After"), which can be assigned to the (003), (006), and (012) crystal planes of hexagonal hydrated metal hydroxide, matching well with those of $Ni(OH)_2 \cdot 0.75H_2O$

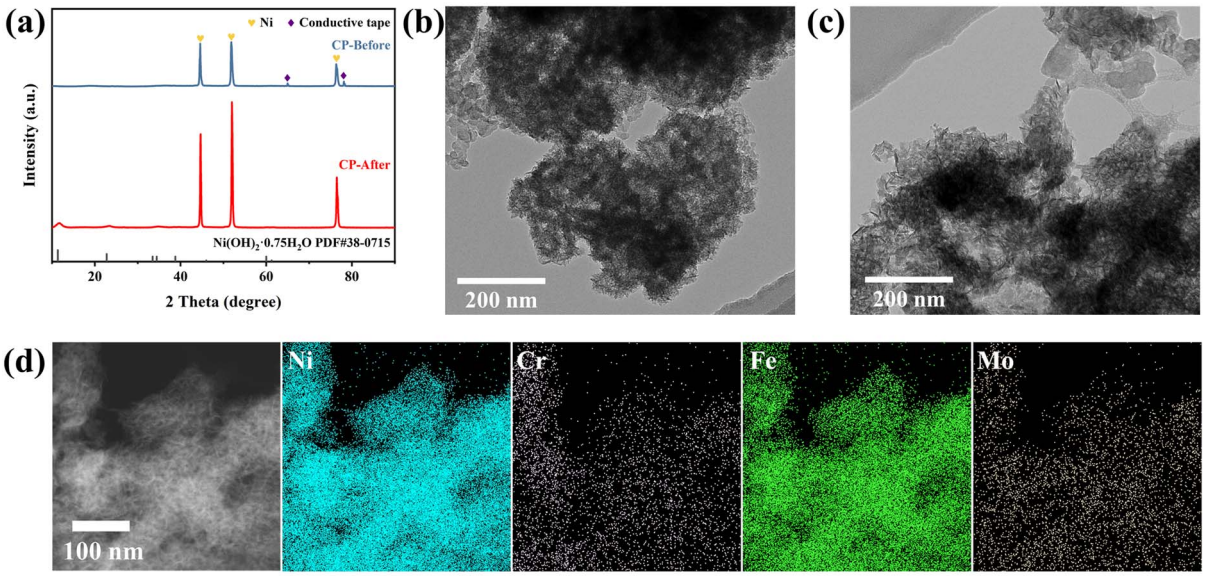

Fig. 4 (a) XRD patterns of NiCrFeMo LDH catalysts before and after the stability test. TEM images of NiCrFeMo LDH catalysts (b) before and (c) after the stability test. (d) TEM-EDS elemental maps of NiCrFeMo LDH catalysts after the stability test.

(JCPDS No. 38-0715). $Ni(OH)_2$ was formed due to spontaneous reduction of NiOOH upon the release of O_2 ($4NiOOH + 2H_2O \rightarrow 4Ni(OH)_2 + O_2 \uparrow$), in accordance with previous reports in the literature.[63–65] TEM imaging revealed that the original nanoporous uniform spherical structure of NiCrFeMo LDHs is not prominent after the stability test (Fig. 4b and c). Instead, the post-OER NiCrFeMo comprises interwoven thin nanosheets (Fig. 4d). Nevertheless, TEM-EDS elemental mapping confirmed that Ni, Cr, Fe and Mo elements remain uniformly distributed across the whole LDH particle, though the intensity of Cr and Mo becomes notably attenuated.

Additionally, the surface chemistry changes of NiCrFeMo LDHs after the stability test were also investigated by XPS. The survey spectra confirm the presence of Ni, Cr and Fe in the sample with attenuated intensity (Fig. 5a), and the signal of Mo is virtually invisible. Besides Mo leaching, such a change is believed to result from the coverage of Nafion residues on the outermost surface of catalysts, which is corroborated by the sharp peaks appearing at 689.1 and 835.1 eV, corresponding to the F 1s and F KLL Auger signals, respectively.[66] High-resolution XPS spectra reveal that there are negligible changes in the oxidation states of Ni and Cr (Fig. 5b and c). However, for the Fe 2p XPS spectrum of the post-OER sample (CP-After), a new pre-peak appears at 706.8 eV (Fig. 5d), which can be attributed to the introduction of defects at adjacent sites, leading to the formation of Fe ions with oxidation states lower than normal.[67] It is hypothesised that these defects might arise from the leaching of Cr and Mo in the LDHs. As for Mo, since its content in NiCrFeMo LDHs is low, no signal of Mo was detected in the post-OER sample (Fig. 5e), implying that it is not existent on the surface of LDHs but still likely present in the interior of LDHs, as evidenced by the TEM-EDS mapping (Fig. 4d). Besides, the O 1s XPS spectrum shows that the M–OH bond dominates in the post-OER sample (Fig. 5f), indicating a weakened covalency of the M–O bond.[68,69]

To quantify the metal leaching from NiCrFeMo LDHs upon the stability test at high current densities (*i.e.*, 500 mA cm^{-2}), ICP-MS analysis was conducted for both the post-OER catalyst and the electrolyte. As shown in Fig. S11a (ESI),† the Ni, Cr, and

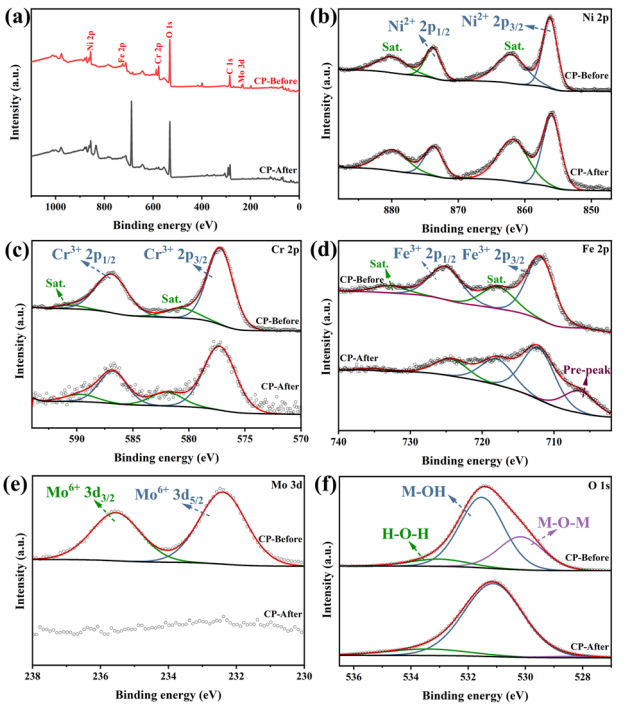

Fig. 5 XPS characterization of NiCrFeMo LDH catalysts before and after the stability test. (a) Survey spectra and high-resolution (b) Ni 2p, (c) Cr 2p, (d) Fe 2p, (e) Mo 3d, and (f) O 1s XPS spectra.

Fe contents become dissimilar being 41.7 : 28.8 : 29.2, and the Mo content is significantly reduced to just 0.3%, in line with the above TEM-EDS and XPS results. Accordingly, the dissolved metal contents in the electrolyte show the opposing trend, with the Mo content amounting to 83.2% and Ni content to 0.3% (Fig. S11b, ESI†). The ICP-MS results suggest that the Ni in NiCrFeMo LDHs is much more stable than other elements under operation conditions, and Cr and Fe have relatively good electrochemical stability, while Mo is susceptible to leaching.

3.3 OER mechanism analyses

The adsorbate evolution mechanism has been widely adopted to describe the OER process in alkaline media, which involves four concerted proton-coupled electron transfer steps at the transition metal active sites (Fig. 6a). In recent years, the lattice oxygen-mediated mechanism (LOM) was also extensively studied in oxides and hydroxides,[38,70–73] which arises from the redox process of lattice oxygen anions and reversible formation of surface oxygen vacancies (V_O, Fig. 6b).[74–76] Which mechanism predominates during the OER highly depends on the materials and the oxidation state of transition metals therein, and it remains controversial.[77] Although recent research studies suggest that many LDH-based materials follow the LOM pathway and thereby exhibit outstanding OER activity,[78–80] reactions which proceed *via* the LOM may deteriorate structural intactness of catalysts, leading to poor long-term stability; moreover, whether the LOM applies to all LDH catalysts remains elusive.

To elucidate the reaction mechanism of NiCrFeMo LDHs, DEMS experiments were performed. Before the DEMS test, NiCrFeMo LDHs were first labelled with $H_2{}^{18}O$ in 0.1 M KOH (see Section 2.5) and then tested in $H_2{}^{16}O$-based 0.1 M KOH. Typically, if the OER taking place on the catalyst follows the adsorbate evolution mechanism, then the signal from $^{16}O^{16}O$ ($m/z = 32$) should predominate, with a trace signal of $^{18}O^{16}O$ ($m/z = 34$) but no signal of $^{18}O^{18}O$ ($m/z = 36$).[81–83] In contrast, in case the LOM plays a major role, the mass spectrometer will be able to detect signals of all oxygen species (*i.e.*, $^{16}O^{16}O$, $^{18}O^{16}O$, and $^{18}O^{18}O$).[82–84] As seen in Fig. 6c, when performing cyclic voltammetry, very strong signals (blue trace) of $^{16}O^{16}O$ can be detected synchronically with the CV cycles. Moreover, there are only very weak signals of $^{18}O^{16}O$ (green trace) appearing, and no

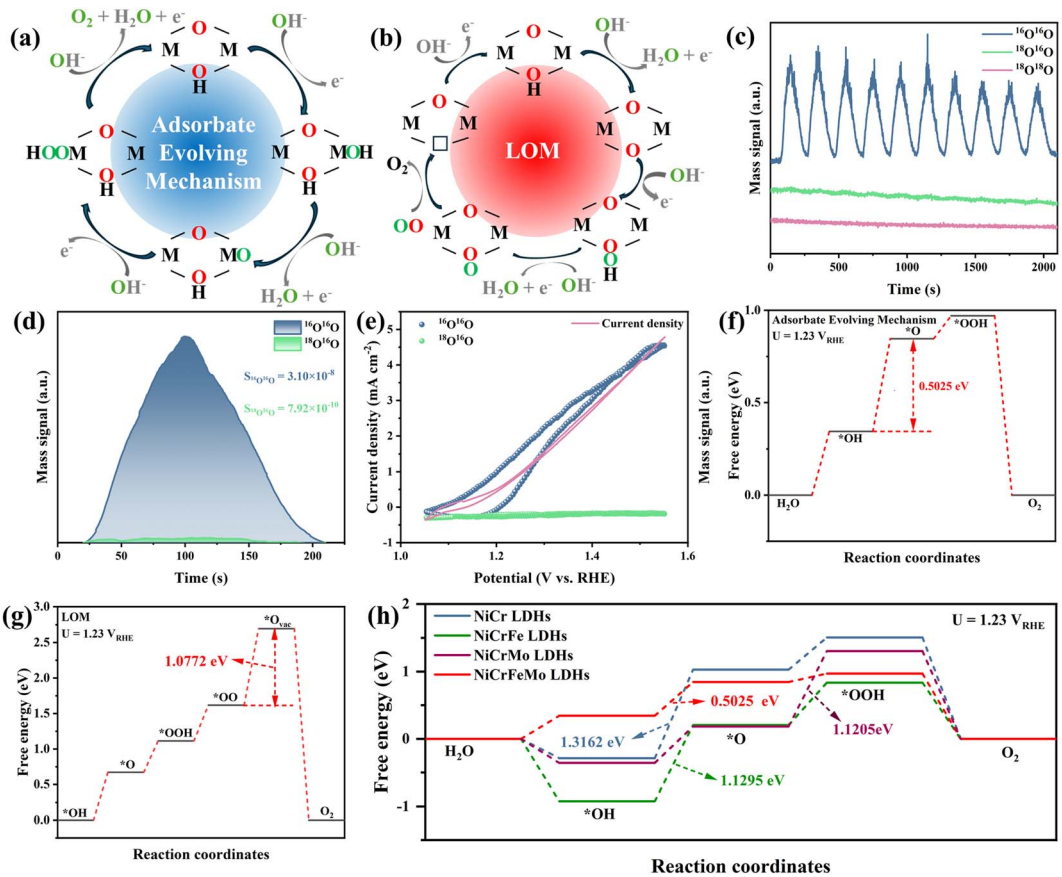

Fig. 6 Mechanistic and theoretical analyses of NiCrFeMo LDHs towards the OER. Schemes illustrating the (a) adsorbate evolution mechanism and (b) LOM pathways on (NiCrFeMo)OOH. (c) DEMS isotope labelling test. (d) DEMS signals of $^{34}O_2$ ($^{18}O^{16}O$) and $^{32}O_2$ ($^{16}O^{16}O$) from the produced oxygen gas by the ^{18}O-labelled NiCrFeMo LDH catalysts tested in 0.1 M KOH electrolyte containing $H_2{}^{16}O$. (e) DEMS signals of $^{34}O_2$ ($^{18}O^{16}O$) and $^{32}O_2$ ($^{16}O^{16}O$) as a function of the applied potential. Gibbs free energy diagram of the OER process following the (f) adsorbate evolution mechanism pathway and (g) LOM pathway. (h) Gibbs free energy diagrams of various LDH-based catalysts for the OER *via* the adsorbate evolution mechanism pathway.

signals of $^{18}O^{18}O$ (pink trace) are discerned, indicating that the OER occurring on NiCrFeMo LDHs predominantly follows the adsorbate evolution mechanism. This is further corroborated by the integrated intensity profiles of $^{16}O^{16}O$ and $^{18}O^{16}O$ signals (Fig. 6d), where the integration of $^{16}O^{16}O$ overwhelms that of $^{18}O^{16}O$ with a large ratio of 39 : 1. When comparing the mass signals of $^{16}O^{16}O$ with those of $^{18}O^{16}O$ within one CV cycle, the same trend is observed (Fig. 6e).

Furthermore, DFT calculations were carried out to understand the OER mechanism of multimetallic NiCrFeMo LDHs. In previous studies,[85–87] materials like NiFe and NiFeCo oxides/hydroxides have been utilised as OER electrocatalysts alone or as precursors to design multimetallic catalysts. Although the identification of active sites is still under debate, it is generally accepted that the *in situ* formed NiOOH upon applying an anodic potential is the main electrocatalytically active species and plays an important role in enhancing the OER activity.[88] Recently, Liu *et al.* calculated the adsorption energies of OER intermediates on various transition metal sites and confirmed that Ni sites have the lowest energy barrier for the reaction.[89] Raman spectroscopy is a molecular spectroscopic technique that provides useful information on surface molecular structures.[90] To experimentally verify if the Ni sites in our NiCrFeMo LDHs are the major active sites, we conducted *in situ* Raman spectroscopy experiments and observed the emergence of two peaks at 475 and 547 cm^{-1} as the applied anodic potential increased (Fig. S12, ESI†), characteristic of the E_g bending vibration and A_{1g} stretching vibration of Ni^{3+}–O bonding in γ-NiOOH,[91] respectively. This indicates that Ni serves as the primary active site in NiCrFeMo LDHs. To validate the experimental result, we first calculated the Gibbs free energy of NiCrFeMo LDHs based on the adsorbate evolution mechanism. Considering the layered structure of LDHs, the model catalysts were constructed by exposing the (001) crystal facet where Ni (Fig. S13, ESI†), Fe (Fig. S14, ESI†) and Cr (Fig. S15, ESI†) are designated as the active site, respectively. The results show that when Ni serves as the active site, and the rate-determining step (RDS) is *OH deprotonation with an energy barrier of 0.5025 eV. In contrast, when Fe acts as the active site, O–O bond formation becomes the RDS exhibiting a significantly higher energy barrier of 1.2953 eV compared to the case of the Ni active site (Fig. S16, ESI†). It is interesting to note that if Cr is assigned to the active site, the OH species adsorbed on Cr would spontaneously migrate to the neighbouring Ni site (Fig. S15, ESI†), implying that Cr itself is not hydroxyl-philic and cannot serve as the active site in NiCrFeMo LDHs. It is also worth mentioning that since the Mo content in NiCrFeMo is low (Fig. 1c), we did not designate Mo as the active site.

Taking the above results into account, in subsequent calculations we only assign Ni as the active site in all model catalysts (Fig. S17–S20, ESI†). First, we compared the Gibbs free energy diagram of NiCrFeMo LDHs based on the adsorbate evolution mechanism to that of the same material along the LOM pathway (Fig. 6f and g). As mentioned above, the former shows a small energy barrier of 0.5025 eV, while the RDS for the LOM is the desorption of *OO and the formation of the O_{vac} site that exhibits a remarkably larger energy barrier of 1.0772 eV. This suggests that the OER would prefer to proceed through the adsorbate evolution mechanism, which rationally explains the above ^{18}O-labelled DEMS results. To further elucidate the synergistic effects among various metals and the advantage of the combination of Ni, Fe, Cr, and Mo elements, DFT calculations were also performed to compare Gibbs free energy changes (ΔG) during the OER *via* the adsorbate evolution mechanism for NiCr, NiCrFe, NiCrMo, and NiCrFeMo LDHs (Fig. 6h). The RDS for NiCr LDHs, NiCrFe LDHs, and NiCrFeMo LDHs is *OH deprotonation, with energy barriers of 1.3162 eV, 1.1295 eV, and 0.5025 eV, respectively, showing a descending trend as the number of metal species increases. In contrast, for NiCrMo LDHs, the RDS involves the transformation of *O into *OOH *via* OH adsorption, with an energy barrier of 1.1205 eV. These theoretical calculations manifest that NiCrFeMo LDHs show the lowest reaction energy barrier and the best OER activity, consistent with our experimental observations.

3.4 Anion exchange membrane water electrolysis performance

To verify the potential of NiCrFeMo LDH electrocatalysts for practical applications, an anion exchange membrane water electrolyser (AEMWE) was assembled using NiCrFeMo LDHs as the anode catalyst and commercial Pt/C as the cathode catalyst (Fig. 7a). NiCrFeMo LDHs and Pt/C were loaded on a woven nickel mesh and carbon paper, respectively, to minimise polarisation losses. The AEMWE can achieve a current density of 1 A cm^{-2} at 1.87 V (Fig. 7b), outperforming the cell comprising commercial RuO_2 as the anode catalyst (1 A cm^{-2}@2.12 V). Additionally, the NiCrFeMo LDHs demonstrated stable operation at a constant current density of 500 mA cm^{-2} for 100 h (Fig. 7c). The minor fluctuations observed arise from the temperature change caused by the supplement of water to the constant-temperature water bath. The measurement

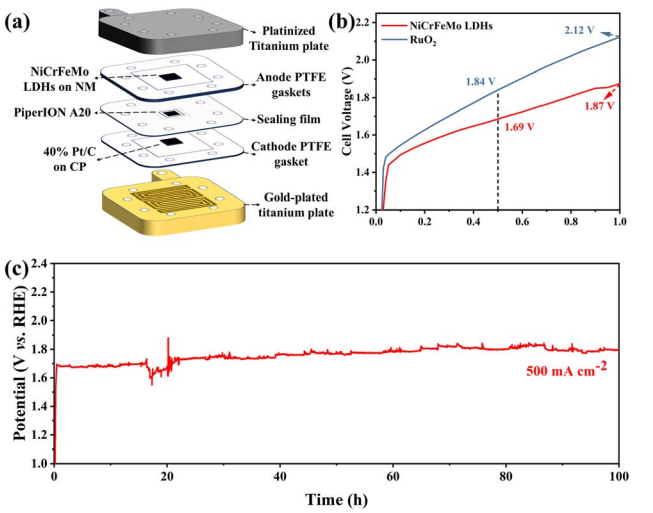

Fig. 7 (a) Schematic illustration of the home-made single-cell AEM electrolyser. (b) Polarisation curve of the AEMWE single cell. (c) Stability of the AEMWE single cell tested at 500 mA cm^{-2}.

demonstrates the viability of NiCrFeMo LDHs for use as cost-effective, high-performance anode catalysts in AEMWE.

4. Conclusions

In conclusion, we successfully synthesised multimetallic NiCrFeMo LDH electrocatalysts through a fast microwave-assisted hydrothermal method. Our comprehensive physicochemical characterisation reveals the synergy among different metals in LDHs. The introduction of Fe helps to increase the oxidation state of other metal elements, while the addition of high-valence Mo tends to decrease the oxidation state of other metals. Consequently, NiCrFeMo LDHs exhibit OER performance much better than that of their binary and ternary counterparts, and are able to achieve 500 mA cm^{-2} at a comparatively low overpotential of 387 mV. Moreover, NiCrFeMo LDHs can sustain continuous OER at such a high industry-relevant current density for 1000 hours, showing outstanding long-term stability. Both DEMS experiments and DFT calculations confirm that the OER occurring on NiCrFeMo LDHs prefers to proceed *via* the adsorbate evolution mechanism, thereby rationally explaining the exceptional durability of this catalyst. Importantly, we demonstrate that NiCrFeMo LDHs can be deployed as anode catalysts in MEAs, exhibiting favorable electrochemical performance in practical devices, which show substantial promise for use in efficient and cost-effective AEMWE in the future.

Data availability

Data will be made available on request.

Author contributions

Yaowen Xu: methodology, investigation, data curation, formal analysis, writing – original draft. Kaiyang Xu: methodology, software, validation, formal analysis. Hao Tan: formal analysis. Haoliang Huang: investigation, formal analysis. Fei Lin: formal analysis. Chenyue Zhang: methodology. Jingwei Wang: formal analysis. Run Ran: formal Analysis. Jinfeng Zeng: formal analysis. Zhipeng Yu: investigation. Sitaramanjaneya Mouli Thalluri: investigation. Lijian Meng: formal analysis. Dehua Xiong: supervision, resources, funding acquisition. Lifeng Liu: writing – review & editing, supervision, resources, project administration, funding acquisition, formal analysis, conceptualization. All authors commented on the final manuscript.

Conflicts of interest

The authors declare that they have no known competing financial interests or personal relationships that could have appeared to influence the work reported in this paper.

Acknowledgements

L. Liu acknowledges the financial support from the Ministry of Science and Technology of China through the National Key R&D Program (Grant No. 2024YFE0114900) and Talent Recruitment Program (Grant No. 22J4021Z311) as well as the Start-Up Grant offered by Songshan Lake Materials Laboratory (Grant No. Y2D1051Z311). D. H. Xiong is grateful for the support by the Open Research Fund of Songshan Lake Materials Laboratory (Grant No. 2023SLABFN11). The authors thank Diamond Light Source for instrument access on B18 (SP36104) and the beamline scientist Veronica Celorrio for her assistance.

Notes and references

1 P. L. Zhai, C. Wang, Y. Y. Zhao, Y. X. Zhang, J. F. Gao, L. C. Sun and J. A. Hou, *Nat. Commun.*, 2023, **14**, 1873.
2 Y. Wang, S. Wang, Z. L. Ma, L. T. Yan, X. B. Zhao, Y. Y. Xue, J. M. Huo, X. Yuan, S. N. Li and Q. G. Zhai, *Adv. Mater.*, 2022, **34**, 2107488.
3 C. Wang, P. L. Zhai, M. Y. Xia, Y. Z. Wu, B. Zhang, Z. W. Li, L. Ran, J. F. Gao, X. M. Zhang, Z. Z. Fan, L. C. Sun and J. G. Hou, *Angew. Chem., Int. Ed.*, 2021, **60**, 27126–27134.
4 P. Liu, B. Chen, C. W. Liang, W. T. Yao, Y. Z. Cui, S. Y. Hu, P. C. Zou, H. Zhang, H. J. Fan and C. Yang, *Adv. Mater.*, 2021, **33**, 2007377.
5 J. Zhao, N. Liao and J. Luo, *J. Mater. Chem. A*, 2023, **11**, 9682–9690.
6 L. G. Li, P. T. Wang, Q. Shao and X. Q. Huang, *Chem. Soc. Rev.*, 2020, **49**, 3072–3106.
7 S. Sun, X. Zhou, B. Cong, W. Hong and G. Chen, *ACS Catal.*, 2020, **10**, 9086–9097.
8 N. Zhang, X. B. Feng, D. W. Rao, X. Deng, L. J. Cai, B. C. Qiu, R. Long, Y. J. Xiong, Y. Lu and Y. Chai, *Nat. Commun.*, 2020, **11**, 4066.
9 Y. L. Zhu, H. A. Tahini, Z. W. Hu, Z. G. Chen, W. Zhou, A. C. Komarek, Q. Lin, H. J. Lin, C. T. Chen, Y. J. Zhong, M. T. Fernández-Díaz, S. C. Smith, H. T. Wang, M. L. Liu and Z. P. Shao, *Adv. Mater.*, 2020, **32**, 1905025.
10 J. Zhou, L. J. Zhang, Y. C. Huang, C. L. Dong, H. J. Lin, C. T. Chen, L. H. Tjeng and Z. W. Hu, *Nat. Commun.*, 2020, **11**, 1984.
11 T. G. Yun, Y. Heo, H. B. Bae and S.-Y. Chung, *Nat. Commun.*, 2021, **12**, 824.
12 Z.-F. Huang, J. Song, Y. Du, S. Xi, S. Dou, J. M. V. Nsanzimana, C. Wang, Z. J. Xu and X. Wang, *Nat. Energy*, 2019, **4**, 329–338.
13 P. Li, M. Wang, X. Duan, L. Zheng, X. Cheng, Y. Zhang, Y. Kuang, Y. Li, Q. Ma, Z. Feng, W. Liu and X. Sun, *Nat. Commun.*, 2019, **10**, 1711.
14 D. Wang, Q. Li, C. Han, Q. Lu, Z. Xing and X. Yang, *Nat. Commun.*, 2019, **10**, 3899.
15 L. Tan, H. Wang, C. Qi, X. Peng, X. Pan, X. Wu, Z. Wang, L. Ye, Q. Xiao, W. Luo, H. Gao, W. Hou, X. Li and T. Zhan, *Appl. Catal., B*, 2024, **342**, 123352.
16 I. Amorim and L. F. Liu, *Curr. Opin. Electrochem.*, 2022, **34**, 101031.
17 I. Amorim, J. Xu, N. Zhang, Z. Yu, A. Araujo, F. Bento and L. Liu, *Chem. Eng. J.*, 2021, **420**, 130454.
18 J. Zhou, C. Zhu, Y. Zhou, J. Dong, P. Li, Z. Zhang, Z. Wang, Y.-C. Lin, J. Shi, R. Zhang, Y. Zheng, H. Yu, B. Tang, F. Liu,

L. Wang, L. Liu, G.-B. Liu, W. Hu, Y. Gao, H. Yang, W. Gao, L. Lu, Y. Wang, K. Suenaga, G. Liu, F. Ding, Y. Yao and Z. Liu, *Nat. Mater.*, 2023, **22**, 450–458.

19 I. Amorim, J. Xu, N. Zhang, D. Xiong, S. M. Thalluri, R. Thomas, J. P. S. Sousa, A. Araujo, H. Li and L. Liu, *Catal. Today*, 2020, **358**, 196–202.

20 Y. Li, B. Wei, Z. Yu, O. Bondarchuk, A. Araujo, I. Amorim, N. Zhang, J. Xu, I. C. Neves and L. Liu, *ACS Sustainable Chem. Eng.*, 2020, **8**, 10193–10200.

21 J. Liu, Y. Du, X. Sun, S. Li, Y. Liu and L. Wang, *Nano Energy*, 2025, **133**, 110485.

22 R. Gao, D. P. Yan and X. Duan, *Cell Rep. Phys. Sci.*, 2021, **2**, 100536.

23 L. Lv, Z. X. Yang, K. Chen, C. D. Wang and Y. J. Xiong, *Adv. Energy Mater.*, 2019, **9**, 1803358.

24 Y. Yang, L. Li, G. Ruan, H. Fei, C. Xiang, X. Fan and J. M. Tour, *ACS Nano*, 2014, **8**, 9622–9628.

25 R. Luo, Y. Li, L. Xing, R. Zhong, Z. Qian, G. Yin, Y. Wang and L. Du, *ACS Sustainable Chem. Eng.*, 2022, **311**, 121357.

26 N. Zhang, I. Amorim and L. Liu, *Nanotechnology*, 2022, **33**, 432004.

27 J. Xu, J. Li, D. Xiong, B. Zhang, Y. Liu, K.-H. Wu, I. Amorim, W. Li and L. Liu, *Chem. Sci.*, 2018, **9**, 3470–3476.

28 K. Xu, L. Liang, T. Li, M. Bao, Z. Yu, J. Wang, S. M. Thalluri, F. Lin, Q. Liu, Z. Cui, S. Song and L. Liu, *Adv. Mater.*, 2024, **36**, 2403792.

29 P. S. Li, X. X. Duan, Y. Kuang, Y. P. Li, G. X. Zhang, W. Liu and X. M. Sun, *Adv. Energy Mater.*, 2018, **8**, 1703341.

30 D. W. Wang, Q. Li, C. Han, Q. Q. Lu, Z. C. Xing and X. R. Yang, *Nat. Commun.*, 2019, **10**, 3899.

31 L. Dai, Z. N. Chen, L. X. Li, P. Q. Yin, Z. Q. Liu and H. Zhang, *Adv. Mater.*, 2020, **32**, 1906915.

32 M. S. Xiao, Y. P. Tian, Y. H. Yan, K. Feng and Y. Q. Miao, *Electrochim. Acta*, 2015, **164**, 196–202.

33 M. W. Louie and A. T. Bell, *J. Am. Chem. Soc.*, 2013, **135**, 12329–12337.

34 M. S. Burke, L. J. Enman, A. S. Batchellor, S. Zou and S. W. Boettcher, *Chem. Mater.*, 2015, **27**, 7549–7558.

35 L. Wang, C. Lin, F. Zhang and J. Jin, *ACS Nano*, 2014, **8**, 3724–3734.

36 L. Trotochaud, S. L. Young, J. K. Ranney and S. W. Boettcher, *J. Am. Chem. Soc.*, 2014, **136**, 6744–6753.

37 B. Zhang, L. Wang, Z. Cao, S. M. Kozlov, F. P. G. de Arquer, C. T. Dinh, J. Li, Z. Y. Wang, X. L. Zheng, L. S. Zhang, Y. Z. Wen, O. Voznyy, R. Comin, P. De Luna, T. Regier, W. L. Bi, E. E. Alp, C. W. Pao, L. R. Zheng, Y. F. Hu, Y. J. Ji, Y. Y. Li, Y. Zhang, L. Cavallo, H. S. Peng and E. H. Sargent, *Nat. Catal.*, 2020, **3**, 985–992.

38 Y. Y. Zhai, X. R. Ren, Y. Sun, D. Li, B. L. Wang and S. Liu, *ACS Sustainable Chem. Eng.*, 2023, **323**, 122091.

39 D. Xu, M. B. Stevens, Y. Rui, G. DeLuca, S. W. Boettcher, E. Reichmanis, Y. Li, Q. Zhang and H. Wang, *Electrochim. Acta*, 2018, **265**, 10–18.

40 Z. Cai, J. Liang, Z. Li, T. Yan, C. Yang, S. Sun, M. Yue, X. Liu, T. Xie, Y. Wang, T. Li, Y. Luo, D. Zheng, Q. Liu, J. Zhao, X. Sun and B. Tang, *Nat. Commun.*, 2024, **15**, 6624.

41 Y. L. Zhu, W. Zhou, Z. G. Chen, Y. B. Chen, C. Su, M. O. Tadé and Z. P. Shao, *Angew. Chem., Int. Ed.*, 2015, **54**, 3897–3901.

42 J. Q. Yan, L. Q. Kong, Y. J. Ji, J. White, Y. Y. Li, J. Zhang, P. F. An, S. Z. Liu, S. T. Lee and T. Y. Ma, *Nat. Commun.*, 2019, **10**, 2149.

43 K. Kuepper, I. Balasz, H. Hesse, A. Winiarski, K. C. Prince, M. Matteucci, D. Wett, R. Szargan, E. Burzo and M. Neumann, *Phys. Status Solidi A*, 2004, **201**, 3252–3256.

44 P. F. Liu, S. Yang, L. R. Zheng, B. Zhang and H. G. Yang, *Chem. Sci.*, 2017, **8**, 3484–3488.

45 Z. Yu, G. D'Olimpio, H. Huang, C.-N. Kuo, C. S. Lue, G. Nicotra, F. Lin, D. W. Boukhvalov, A. Politano and L. Liu, *Adv. Funct. Mater.*, 2024, **34**, 2403099.

46 H. Tan, Z. Yu, A. P. LaGrow, S. Ma, J. Wang, H. Li, D. Xiong and L. Liu, *J. Mater. Chem. A*, 2023, **11**, 26152–26163.

47 S. Y. Ma, J. L. Bai, W. Liao, C. Jiang, Q. Y. Shen, L. F. Liu, X. J. Zhao and D. H. Xiong, *J. Alloys Compd.*, 2024, **1004**, 175795.

48 C. C. L. McCrory, S. Jung, J. C. Peters and T. F. Jaramillo, *J. Am. Chem. Soc.*, 2013, **135**, 16977–16987.

49 Z. Yu, C. Si, A. P. LaGrow, Z. Tai, W. A. Caliebe, A. Tayal, M. J. Sampaio, J. P. S. Sousa, I. Amorim, A. Araujo, L. Meng, J. L. Faria, J. Xu, B. Li and L. Liu, *ACS Catal.*, 2022, **12**, 9397–9409.

50 J. W. Wang, L. J. Cai, Z. P. Yu, H. Tan, X. Y. Xiang, K. Y. Xu, Y. Chao, S. M. Thalluri, F. Lin, H. L. Huang, C. Y. Zhang, Y. Zhao, W. L. Wang and L. F. Liu, *J. Mater. Chem. A*, 2024, **13**, 312–324.

51 X. W. Yu, B. Wang, C. Wang, C. Zhuang, Y. F. Yao, Z. S. Li, C. P. Wu, J. Y. Feng and Z. G. Zou, *Small*, 2021, **17**, 2103412.

52 L. Yu, H. Q. Zhou, J. Y. Sun, I. K. Mishra, D. Luo, F. Yu, Y. Yu, S. Chen and Z. F. Ren, *J. Mater. Chem. A*, 2018, **6**, 13619–13623.

53 Y. P. Lin, H. Wang, C. K. Peng, L. M. Bu, C. L. Chiang, K. Tian, Y. Zhao, J. Q. Zhao, Y. G. Lin, J. M. Lee and L. J. Gao, *Small*, 2020, **16**, 2002426.

54 H. Sun, L. Chen, Y. B. Lian, W. J. Yang, L. Lin, Y. F. Chen, J. B. Xu, D. Wang, X. Q. Yang, M. H. Rümmerli, J. Guo, J. Zhong, Z. Deng, Y. Jiao, Y. Peng and S. Z. Qiao, *Adv. Mater.*, 2020, **32**, 2006784.

55 C. L. Li, Z. J. Zhang and R. Liu, *Small*, 2020, **16**, 2003777.

56 J. Kwon, H. Han, S. Jo, S. Choi, K. Y. Chung, G. Ali, K. Park, U. Paik and T. Song, *Adv. Energy Mater.*, 2021, **11**, 2100624.

57 C. L. Dong, X. T. Yuan, X. Wang, X. Y. Liu, W. J. Dong, R. Q. Wang, Y. H. Duan and F. Q. Huang, *J. Mater. Chem. A*, 2016, **4**, 11292–11298.

58 Y. Y. Zhai, X. R. Ren, Y. Sun, D. Li, B. L. Wang and S. Liu, *ACS Sustainable Chem. Eng.*, 2023, **323**, 122091.

59 X. D. Du, W. Y. Fu, P. Su, Q. Z. Zhang and M. H. Zhou, *J. Environ. Sci.*, 2023, **127**, 652–666.

60 M. Han, C. Wang, J. Zhong, J. Han, N. Wang, A. Seifitokaldani, Y. Yu, Y. Liu, X. Sun, A. Vomiero and H. Liang, *ACS Sustainable Chem. Eng.*, 2022, **301**, 120764.

61 L. Xu, Q. Q. Jiang, Z. H. Xiao, X. Y. Li, J. Huo, S. Y. Wang and L. M. Dai, *Angew. Chem., Int. Ed.*, 2016, **55**, 5277–5281.

62 H. Lei, L. Ma, Q. X. Wan, S. Z. Tan, B. Yang, Z. L. Wang, W. J. Mai and H. J. Fan, *Adv. Energy Mater.*, 2022, **12**, 2202522.
63 J. Wei, Y. F. Shao, J. B. Xu, F. Yin, Z. J. Li, H. T. Qian, Y. P. Wei, L. Chang, Y. Han, J. Li and L. Gan, *Nat. Commun.*, 2024, **15**, 9012.
64 H. Dotan, A. Landman, S. W. Sheehan, K. D. Malviya, G. E. Shter, D. A. Grave, Z. Arzi, N. Yehudai, M. Halabi, N. Gal, N. Hadari, C. Cohen, A. Rothschild and G. S. Grader, *Nat. Energy*, 2019, **4**, 786–795.
65 D. D. Macdonald and M. L. J. J. o. T. E. S. Challingsworth, *J. Electrochem. Soc.*, 1993, **140**, 606.
66 O. Bondarchuk, A. P. LaGrow, A. Kvasha, T. Thieu, E. Ayerbe and I. Urdampilleta, *Appl. Surf. Sci.*, 2021, **535**, 147699.
67 H. Zhao, Y. Wang, Y. Wang, T. Cao and G. Zhao, *Appl. Catal., B*, 2012, **125**, 120–127.
68 T. X. Nguyen, C. C. Tsai, V. T. Nguyen, Y.-J. Huang, Y.-H. Su, S.-Y. Li, R.-K. Xie, Y. J. Lin, J.-F. Lee and J.-M. Ting, *Chem. Eng. J.*, 2023, **466**, 143352.
69 Y. Yang, Y. Ou, Y. Yang, X. Wei, D. Gao, L. Yang, Y. Xiong, H. Dong, P. Xiao and Y. Zhang, *Nanoscale*, 2019, **11**, 23296–23303.
70 P. L. Zhai, C. Wang, Y. Y. Zhao, Y. X. Zhang, J. F. Gao, L. C. Sun and J. A. Hou, *Nat. Commun.*, 2023, **14**, 1873.
71 L. Zhou, D. Y. Guo, L. H. Wu, Z. X. Guan, C. Zou, H. L. Jin, G. Y. Fang, X. Chen and S. Wang, *Nat. Commun.*, 2024, **15**, 2481.
72 W. H. Antink, S. B. Lee, H. S. Lee, H. Shin, T. Y. Yoo, W. J. Ko, J. Shim, G. M. Na, Y. E. Sung and T. Hyeon, *Adv. Funct. Mater.*, 2024, **34**, 2309438.
73 F. Q. Wang, P. C. Zou, Y. Y. Zhang, W. L. Pan, Y. Li, L. M. Liang, C. Chen, H. Liu and S. J. Zheng, *Nat. Commun.*, 2023, **14**, 6019.
74 A. Grimaud, W. T. Hong, Y. Shao-Horn and J. M. Tarascon, *Nat. Mater.*, 2016, **15**, 121–126.
75 X. Rong, J. Parolin and A. M. Kolpak, *ACS Catal.*, 2016, **6**, 1153–1158.
76 J. S. Yoo, X. Rong, Y. Liu and A. M. Kolpak, *ACS Catal.*, 2018, **8**, 4628–4636.
77 L.-B. Liu, C. Yi, H.-C. Mi, S. L. Zhang, X.-Z. Fu, J.-L. Luo and S. Liu, *Electrochem. Energy Rev.*, 2024, **7**, 14.
78 F. Wang, P. Zou, Y. Zhang, W. Pan, Y. Li, L. Liang, C. Chen, H. Liu and S. Zheng, *Nat. Commun.*, 2023, **14**, 6019.
79 P. Zhai, C. Wang, Y. Zhao, Y. Zhang, J. Gao, L. Sun and J. Hou, *Nat. Commun.*, 2023, **14**, 1873.
80 C. Wang, P. Zhai, M. Xia, Y. Wu, B. Zhang, Z. Li, L. Ran, J. Gao, X. Zhang, Z. Fan, L. Sun and J. Hou, *Angew. Chem., Int. Ed.*, 2021, **60**, 27126–27134.
81 H. Y. Jin, X. Y. Liu, P. F. An, C. Tang, H. M. Yu, Q. H. Zhang, H. J. Peng, L. Gu, Y. Zheng, T. S. Song, K. Davey, U. Paik, J. C. Dong and S. Z. Qiao, *Nat. Commun.*, 2023, **14**, 354.
82 Z.-H. Yin, Y. Huang, K. Song, T.-T. Li, J.-Y. Cui, C. Meng, H. Zhang and J.-J. Wang, *J. Am. Chem. Soc.*, 2024, **146**, 6846–6855.
83 T. Y. Zhang, J. J. Jiang, W. M. Sun, S. Y. Gong, X. W. Liu, Y. Tian and D. S. Wang, *Proc. Natl. Acad. Sci. U. S. A.*, 2024, **121**, e2317247121.
84 Y. Feng, H. Wang, K. Feng, C. Y. Li, S. Li, C. Lu, Y. Y. Li, D. Ma and J. Zhong, *ACS Nano*, 2024, **18**, 28924–28935.
85 D. Wang, Z. Liu, S. Du, Y. Zhang, H. Li, Z. Xiao, W. Chen, R. Chen, Y. Wang, Y. Zou and S. Wang, *J. Mater. Chem. A*, 2019, **7**, 24211–24216.
86 Z. Lu, L. Qian, Y. Tian, Y. Li, X. Sun and X. Duan, *Chem. Commun.*, 2016, **52**, 908–911.
87 Q. Zhang, N. M. Bedford, D. Pan, X. Lu and R. Amal, *Adv. Energy Mater.*, 2019, **9**, 1901312.
88 X. Bo, R. K. Hocking, S. Zhou, Y. B. Li, X. J. Chen, J. C. Zhuang, Y. Du and C. Zhao, *Energy Environ. Sci.*, 2020, **13**, 4225–4237.
89 F. Q. Wang, P. C. Zou, Y. Y. Zhang, W. L. Pan, Y. Li, L. M. Liang, C. Chen, H. Liu and S. J. Zheng, *Nat. Commun.*, 2023, **14**, 6019.
90 C. J. Hu, Y. F. Hu, B. W. Zhang, H. W. Zhang, X. J. Bao, J. J. Zhang and P. Yuan, *Electrochem. Energy Rev.*, 2024, **7**, 19.
91 M. W. Louie and A. T. Bell, *J. Am. Chem. Soc.*, 2013, **135**, 12329–12337.